REVIEW

🔴 Check for updates

Electrochemical investigations of metal nanostructure growth with single crystals

Myung Jun Kim, ![ID]† Micah Brown ![ID]† and Benjamin J. Wiley ![ID]*

Control over the nanoscopic structure of a material allows one to tune its properties for a wide variety of applications. Colloidal synthesis has become a convenient way to produce anisotropic metal nanostructures with a desired set of properties, but in most syntheses, the facet-selective surface chemistry causing anisotropic growth is not well-understood. This review highlights the recent use of electrochemical methods and single-crystal electrodes to investigate the roles of organic and inorganic additives in modulating the rate of atomic addition to different crystal facets. Differential capacitance and chronocoulometric techniques can be used to extract thermodynamic data on how additives selectively adsorb, while mixed potential theory can be used to observe the effect of additives on the rate of atomic addition to a specific facet. Results to date indicate that these experimental methods can provide new insights into the role capping agents and halides play in controlling anisotropic growth.

1. Introduction

Synthetic control over the shape of metal particles at the nanoscale can be used to create nanostructures with physicochemical properties that are distinct from those of spherical nanoparticles. The use of metal nanostructures has rapidly expanded into numerous research fields and industries, including (electro-)catalysis, electronics, (bio-)chemical devices, and pharmaceuticals.[1–6] Growth of anisotropic nanostructures requires shape-directing agents (*i.e.*, ligands and capping agents) that are thought to adsorb preferentially on metal surfaces during colloidal syntheses and thereby direct growth into the desired morphology.[7–14] The precise role of shape-directing agents is not yet well-understood for many nanostructure syntheses. In order to better control the morphology of metal nanostructures so as to optimize their properties for a specific application, a thorough understanding of the process of metal nanocrystal growth and the specific role of shape-directing agents is essential.

Department of Chemistry, Duke University, 124 Science Drive, Box 90354, Durham, North Carolina 27708, USA. E-mail: benjamin.wiley@duke.edu
†These authors contributed equally to this manuscript.

Myung Jun Kim received his B.S. in Chemical and Biological Engineering from Seoul National University in 2007. He obtained his Ph.D. in Chemical and Biological Engineering from Seoul National University in 2013 under the supervision of Prof. Jae Jeong Kim. He is currently a postdoctoral associate in Prof. Wiley's group at Duke University. His research focuses on electrochemical deposition of metals, the growth mechanism of anisotropic metal nanocrystals, and the applications of metal nanowires to electrochemical engineering.

Myung Jun Kim

Micah Brown obtained his Ph.D. in Analytical Chemistry from the University of North Carolina at Chapel Hill in 2018 and his B.S. in Chemistry from the University of Rochester in 2013. He is currently a postdoctoral associate in Prof. Wiley's lab at Duke University. His research focuses on controlled metal electrodepositions and characterization of metal–ligand interactions during nanocrystal synthesis. His broader research interests include electrocatalysis and the design and characterization of electrochemical sensors/biosensors.

Micah Brown

A variety of analytical methods have been used to characterize how nanostructures grow. The growth mechanism of metal nanocrystals was initially based on microscopic images of dried or frozen nanocrystals at different stages of growth. For example, based on images of the anisotropic growth of silver nanowires over time, it was proposed that polymeric capping agents (*i.e.*, poly(vinyl pyrrolidone), PVP) selectively bind and inhibit atomic addition to the nanowire sides while allowing addition to proceed at the uncapped ends.[15] A cetyltrimethylammonium bromide (CTAB) bilayer was similarly hypothesized to selectively block atomic addition to the sides of growing gold nanorods.[16] Ultraviolet–Visible (UV-Vis) spectroscopy has been used to demonstrate how the reaction environment affects the anisotropic growth kinetics of Au nanorods.[17,18] Spectroscopic techniques such as NMR[19–21] and XPS[22,23] have also been used to characterize the density and structure of ligand layers at nanoparticle surfaces. *In situ* transmission electron microscopy (TEM),[24,25] transmission X-ray microscopy (TXM),[26–28] and dark-field optical microscopy (DFOM),[29,30] have enabled continuous, real-time observation of nanocrystal growth. These visualization techniques can be used to differentiate between growth mechanisms based on oriented attachment (*i.e.*, growth *via* attachment of nanoparticles) and atomic addition. DFOM can further differentiate between mass transfer-limited and charge transfer-limited atomic addition for Cu nanowire growth.[29,31]

Despite the large number of experimental studies of nanostructure growth, the facet-selective surface chemistry that drives anisotropic growth of metals with centrosymmetric crystal structures remains poorly understood. One of the most commonly invoked hypotheses for why anisotropic growth occurs is the capping agent hypothesis, which suggests that an organic additive selectively blocks atomic addition to certain facets. However, as of yet, there is no direct experimental evidence for the capping agent hypothesis, nor does the hypothesis account for the role of halides, which are necessary for nanostructure growth in a wide range of syntheses.[32–41] This situation highlights the need for new experimental tools and methods capable of characterizing the facet-selective chemistry that leads to anisotropic nanostructures.

The reactions that govern anisotropic growth of metal nanostructures, which involve transfer of electrons from a reducing agent to metal ions, are electrochemical in nature. Therefore, it is intuitive for electroanalytical methods to be brought to bear on the mechanism of anisotropic growth. Critical to the application of electrochemical methods are the use of single-crystal metal electrodes, which can be used to represent the surface of nanocrystal facets and allow facet-specific phenomena to be observed *in situ* (*i.e.*, in the nanocrystal growth solution). For example, pentagonally-twinned Cu nanowires consist of {111} tip and {100} side facets. Single-crystal Cu(100) and Cu(111) electrodes can be used to probe differences in the rate of atomic addition to these facets in the reaction solution. Using this approach, ligand adsorption and the rate of atomic addition can be directly measured as a function of applied potential, reactant concentrations, and electrode crystallinity. Comparison between the findings on single-crystal electrodes, synthetic results, and computer calculations can then be used to unravel the mechanism for anisotropic growth.[42,43]

This review introduces two categories of electrochemical methods that can be used to analyze the facet-dependent chemistry that causes anisotropic growth of metals: (1) measurement of the surface coverage of shape-directing agents using differential capacitance and/or chronocoulometry (section 2), and (2) measurement of the rate of metal atomic addition using mixed potential theory (section 3).

2. Differential capacitance and chronocoulometric measurements

Preferential ligand adsorption at certain facets of a nanocrystal seed is a common hypothesis for why anisotropic growth of metal nanocrystals occurs.[9,44–52] Implied in these mechanisms is that some facets are more energetically favorable for ligand adsorption than others. This hypothesis has not yet been confirmed experimentally. Historically, obtaining fundamental thermodynamic data (including adsorption isotherms and calculations of the free energy of adsorption) has been the subject of numerous electrochemical investigations of adsorbates on noble metal electrodes.[53–59] Translation of the findings collected on metal electrodes using electrochemical methods to metal nanoparticles seems logical, but the application of these methods to modern-day capping agents is rare. This may be in part due to a lack of widespread understanding of the fundamental thermodynamic principles at play and the appropriate experimental procedures required to observe them. Herein, we seek to provide a brief framework for obtaining thermodynamic data concerning metal–ligand interactions using differential capacity (DC) and chronocoulometric tech-

Benjamin J. Wiley

Benjamin J. Wiley is an Associate Professor in the Department of Chemistry at Duke University. He received his B.S. in Chemical Engineering from the University of Minnesota in 2003, and his Ph.D. in Chemical Engineering from the University of Washington, Seattle in 2007. Prof. Wiley is the recipient of the Beilby Metal from the Royal Society of Chemistry and has been recognized as a Highly Cited Researcher by Thomson Reuters in 2014 and 2018. His current research focuses on understanding the processes that drive anisotropic growth of nanostructures, and understanding the structure–property relationship of nanostructures and for applications in electronics, medicine, and electrochemistry.

View Article Online

Nanoscale

Review

Published on 05 November 2019. Downloaded by Duke University on 2/25/2020 3:03:28 PM.

niques with references to pivotal works and recent applications to nanocrystal growth.

2.1. Theory and methodology

Some of our first notions of how molecules adsorb at electrified metal–solution interfaces were based on measurements of differential capacitance.[60–62] Considering the double layer of an ideally polarized electrode as a parallel plate capacitor in series with the solution resistance, the capacitance varies according to eqn (1), where A is the electrode area, ε_0 is the permittivity of free space, ε_r is the relative permittivity, and d is the distance between the electrode surface and the outer Helmholtz plane (the distance of closest approach for solvated ions).

$$C = \frac{A\varepsilon_0\varepsilon_r}{d} \qquad (1)$$

Adsorption of organic ligands from an aqueous phase generally reduces the value of ε_r and increases d, thus reducing capacitance. The capacitance is measured within the electrode's potential window (boundaries set by solvent electrolysis or electrode corrosion) both in the absence and presence of ligands. Typically, the current arising from a slow dc sweep (0.1–10 mV s^{-1}) overlaid with a small ac perturbation (e.g., 5 mV rms, 25 Hz) can be used in concert with a lock-in amplifier or electrochemical impedance spectrometer to determine the equivalent RC circuit.[60]

Extraction of thermodynamic data from DC traces is possible for low melting point and liquid metal electrodes (e.g., the dropping mercury electrode, DME).[63,64] However, single-crystal noble metal electrodes undergo surface reconstructions during potential sweeps, manifested as a hysteresis in the DC trace. These surface reconstructions may occur at different electrode polarizations depending on the presence of surface-adsorbed species, thus making it difficult to perform background subtractions.[65] As a result, the DC trace is most often collected as a qualitative indicator of metal–ligand surface phenomena. Notably, two key potentials can be roughly determined from DC traces: (1) the potential of zero charge (E_{pzc}), where capacitance is lowest, the surface charge is near-zero, and the most ligand is assumed to be adsorbed; and (2) the desorption potential (E_{des}), where all ligand is removed from the surface and the DC trace begins to overlap with the background electrolyte.

Chronocoulometric analysis can be used as an alternative to DC to measure equilibrium surface charge density and extract meaningful thermodynamic data from solid electrodes using the electrocapillary equation (eqn (2)).[53,63,66]

$$-d\gamma = \sigma_M dE + \sum_i \Gamma_i d\mu_i \qquad (2)$$

Originally derived from the Gibbs adsorption isotherm for the DME-electrolyte interface, the electrocapillary equations relates changes in surface tension (γ) to surface charge density (σ_M) and surface excesses (Γ). The surface excess Γ_i of component i is the difference between the concentration of component i at the surface and the bulk. The value of Γ_i is positive if the concentration of component i is greater at the surface than in the bulk, negative if lower, and zero if equivalent.

Fig. 1 provides an overview of the data collection and analysis procedure for the adsorption of cyclohexanol on polycrystalline Au (one of the first applications of the technique on a solid electrode).[67] Briefly, a variable interrogating potential (E_i) is applied to an electrode for a period of time sufficient for surface processes to have achieved equilibrium. Upon switching the potential to E_{des}, the current transient is collected (Fig. 1a), converted to charge (Fig. 1b), and extrapolated to $t = 0$ (a requirement due to the finite sampling frequency of the instrument). The resulting σ_M values are then plotted against E_i (Fig. 1c). Such σ_M–E traces are collected across a series of relevant ligand concentrations as well as in ligand-free electrolyte. Integration of these traces with respect to potential yields the surface tension. The surface pressure (π) is the difference between the surface tensions in the ligand-containing ($0 < \theta \leq 1$) and ligand-free ($\theta = 0$) trials (eqn (3) and Fig. 1d).

$$\pi = \gamma_{\theta=0} - \gamma_\theta = \int_{E_{des}}^{E_i} \sigma_{M_\theta} dE - \int_{E_{des}}^{E_i} \sigma_{M_{\theta=0}} dE \qquad (3)$$

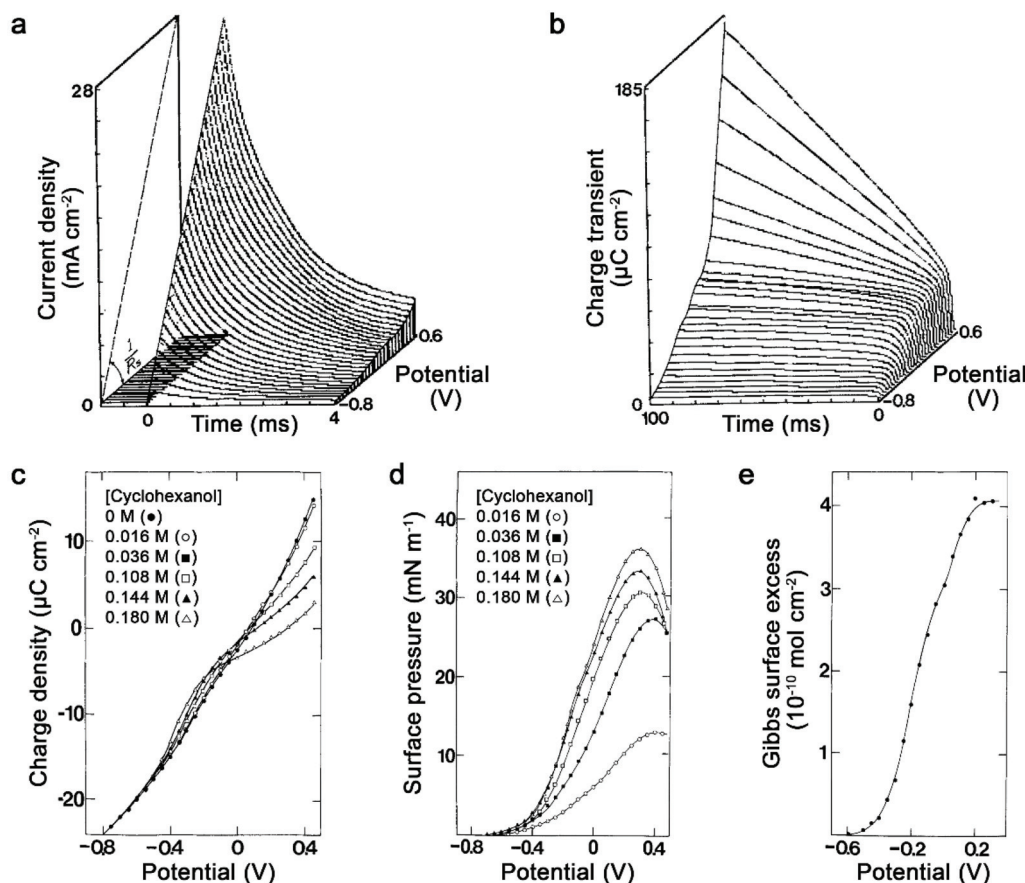Partial differentiation of π with respect to the chemical potential (i.e., RT ln c) yields the Gibbs surface excess according to eqn (4) (Fig. 1e).

$$\Gamma = \left(\frac{\partial\pi}{RT\partial\ln c} \right)_{T,P,E} \qquad (4)$$

In the end, Γ–E adsorption isotherms across different ligand concentrations are plotted on a "rational" potential scale in reference to the electrode's potential of zero charge ($E - E_{pzc}$). Comparison of the adsorption isotherms of different ligands indicates which surface-ligand interaction is most thermodynamically favorable at a given potential. When multiple ligands are present simultaneously, adsorption isotherms may also be used to distinguish between competitive and cooperative effects (see section 2.2). Surface charge σ_M may also be used in place of potential as the independent electric variable.[68] We invite the reader to consult more detailed explanations of the theory and use of the electrocapillary equation for solid, ideally polarized electrodes available in the literature.[61,65,69]

### 2.2. Quaternary ammonium ligands for Au nanorod growth

The quaternary ammonium (QA) surfactant cetyltrimethylammonium bromide (CTAB) is routinely used as a stabilizing ligand for Au nanoparticles and is the favored ligand for syntheses of Au nanorods.[18] The exact mechanism responsible for anisotropic growth for CTAB-stabilized Au nanorods is still debated in the literature, but the presence of the bromide anion is known to be essential.[48] A popular hypothesis contends that the preferential adsorption of QA ligands on certain facets of the seed crystal directs anisotropic growth. However, there is no direct physical evidence to support this hypothesis.

This journal is © The Royal Society of Chemistry 2019

Nanoscale, 2019, **11**, 21709–21723 | **21711**

Fig. 1 (a) Current and (b) charge transients collected in the presence of 0.04 M KClO$_4$ and cyclohexanol on a polycrystalline Au electrode. (c) Surface charge density *versus* potential and (d) surface pressure *versus* potential plots from the data presented in 1b in the presence of 0.04 M KClO$_4$ and cyclohexanol. (e) Gibbs surface excess *versus* potential curve for the 0.180 M hexanol solution presented in (d). Reproduced with permission from ref. 67. Copyright 1986 The Electrochemical Society.

Vivek and Burgess have meticulously characterized the coadsorption of octyltrimethylammonium (OTA$^+$) and bromide anion (Br$^-$) on both Au(111) and Au(100) surfaces with various electrochemical techniques.[70–73] Initial cyclic voltammetry (CV) and DC (Fig. 2a) measurements were used to qualitatively observe the adsorption of each species.[70] Distinct wave features were assigned to interfacial phenomena, including: ligand adsorption, desorption, phase changes, and aggregation. The authors, however, duly warn against overinterpretation of these data, as they do not strictly correspond to states of adsorption equilibria. Sharp peaks corresponding to potential-induced lifting of surface reconstructions—(1 × 23) and (5 × 20) for Au(111) and Au(100), respectively—complicated surface comparisons and motivated the use of chronocoulometric analysis. Notably, at potentials more negative than −0.8 V *vs.* SCE, the CV and DC traces in the presence of OTA$^+$ and/ or Br$^-$ overlapped with traces of the background electrolyte, signifying complete ion desorption (Fig. 2a). The use of these surface-clearing potentials is necessary for chronocoulometric analysis, in which only *changes* in surface charge density are measured.

As detailed in section 2.1, chronocoulometric analysis can be used to determine the surface excesses of individual or coadsorbed ligands at ideally polarized, solid electrodes based on the electrocapillary equation.[53,65] When more than one ligand is present, measurements of this kind allow one to discern between cooperative and competitive adsorption. Moreover, greater surface excess of a ligand on one crystal facet over another constitutes thermodynamic evidence of preferential adsorption. For coadsorbed species, one ligand is held at a constant concentration while σ_M–E plots are collected repeatedly over a range of concentrations of the other ligand.[74] A similar data series is collected with the ligands exchanged. After completing data acquisition and analysis, the resulting ligand adsorption isotherms may be compared in the presence and absence of coadsorbates in order to discern cooperative or competitive effects. For instance, Fig. 2b displays the adsorption isotherms of OTA$^+$ on Au(111) in isolation (*i.e.*, with the inert counteranion triflate, Tf) and in the presence of 1.0 mM NaBr.[70] At negative surface charges, the OTA$^+$ surface excess is unaffected by Br$^-$; however, at positive charges, Br$^-$ is necessary to stabilize OTA$^+$ and avoid desorption. These results
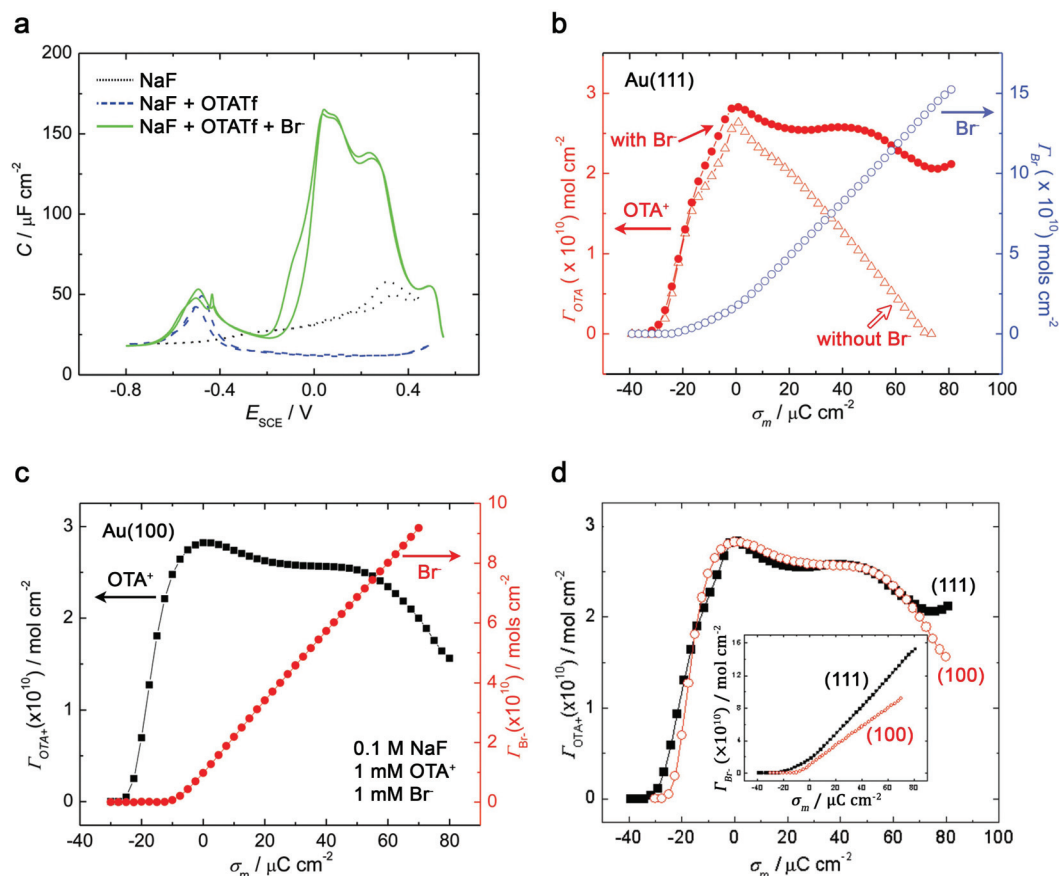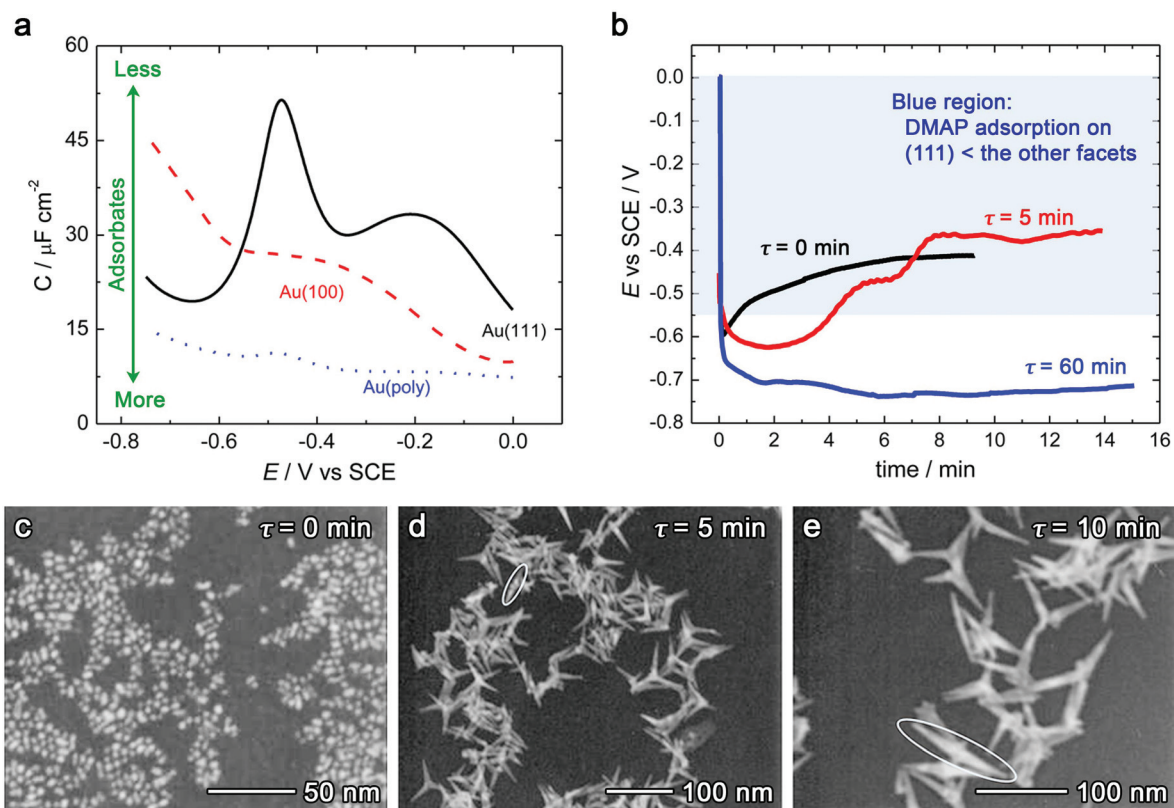
Fig. 2 (a) Differential capacity curves for Au(111) in 0.10 M NaF electrolyte (black dotted) and 1.0 mM OTATf in the absence and presence of 0.1 mM NaBr. (b) Surface excesses *versus* electrode charge density at the Au(111)/0.1 M NaF interface for 1.0 mM OTA$^+$ in the absence and presence of 1.0 mM NaBr and for 1.0 mM Br$^-$ in the presence of 1.0 mM OTATf. (c) Surface excesses *versus* electrode charge density at the Au(100)/0.1 M NaF interface for 1.0 mM OTA$^+$ in the presence of 1.0 mM NaBr and 1.0 mM Br$^-$ in the presence of 1.0 mM OTATf. (d) Overlaid Au(111) and Au(100) adsorption isotherms for 1.0 mM OTA$^+$ in the presence of 1.0 mM NaBr; (inset) corresponding adsorption isotherms for 1.0 mM Br$^-$ in the presence of 1.0 mM OTATf. (a) and (b) are reproduced with permission from ref. 70. Copyright 2012 American Chemical Society. (c) and (d) are reproduced with permission from ref. 71. Copyright 2012 American Chemical Society.

suggest that the adsorption of Br$^-$ is cooperative in that it shields OTA$^+$ from electrostatic repulsion from the positively-charged electrode. The same chronocoulometric analysis was repeated on Au(100) surfaces (Fig. 2c), and an overlay of the adsorption isotherms reveals that OTA$^+$ in the presence of Br$^-$ adsorbs onto Au(111) and Au(100) in the same manner (Fig. 2d).[71] Therefore, there is no thermodynamic basis for the argument that QA-Br$^-$ ligands preferentially bind to one low-energy crystal facet over the other during Au nanorod formation. However, the authors note that this fact alone is not sufficient to rule out preferential adsorption. Each Au nano-particle seed would have a single electrochemical potential, and because the low-energy crystallographic facets of Au have different potentials of zero charge (E_{pzc} = 270 and 70 mV *vs.* SCE for Au(111) and Au(100), respectively), each facet of the seed particle would have a different surface charge density. Although the Γ–σ_M isotherms are very similar on different single crystals (Fig. 2d), a sufficient difference in charge density between facets would be able to promote preferential

ligand adsorption. Unfortunately, this phenomenon could only be observed if methods to directly measure the electronic state of the Au nanoparticle *in situ* were available.

2.3. 4-(Dimethylamino)pyridine as a shape-directing agent for Au nanocrystals

The molecule 4-(dimethylamino)pyridine (DMAP) can be used as a stabilizing ligand in the synthesis of Au nanostructures.[75] Compared to thiol-containing ligands that covalently bond with Au, weak physisorption of DMAP advantageously allows for facile ligand exchange and postsynthetic functionali-zation.[76] Burgess *et al.* studied the electrosorption of DMAP on polycrystalline Au electrodes *via* DC and chronocoulometry, finding that the ligand's orientation and adsorption/desorp-tion characteristics were highly dependent on both pH and electrode potential (in agreement with its well-characterized parent molecule, pyridine[55,56]).[77] Single-crystal Au electrodes were later used by Burgess *et al.* to further probe DMAP's role as a stabilizing ligand and, potentially, as a growth-directing

Fig. 3 (a) Differential capacity curves of 0.1 M 4-dimethylaminopyridine (DMAP) in 0.05 M NaF collected on Au(100), Au(111), and polycrystalline electrodes. (b) Open-circuit potential transients collected on a Au bead electrode initially in the presence of 4 mL 0.1 M DMAP and 100 μL 0.01 M HAuCl$_4$ before addition of sodium borohydride (NaBH$_4$; 100 μL, 0.01 M) at $\tau = 0$. DMAP and HAuCl$_4$ were allowed to react for a set period of time (τ) before NaBH$_4$ addition: $\tau = 0$ min (black trace), 5 min (red), and 60 min (blue). Transmission electron micrographs of the resulting Au nanoparticles with $\tau =$ (c) 0, (d) 5, and (e) 10 min. Reproduced with permission from ref. 78. Copyright 2012 American Chemical Society.

agent in the synthesis of Au nanoparticles.[78] The DC curve in Fig. 3a displays changes in capacitance as the applied potential was swept negatively in the presence of DMAP on different electrodes. Upon adsorption, organic ligands typically lower the observed capacitance due to their small dielectric constants and large size relative to water (effectively extending the outer Helmholtz plane, eqn (1)). At potentials more positive than −0.55 V *vs.* SCE, more DMAP is adsorbed on Au(100) surfaces than on Au(111) (Fig. 3a). Additionally, the consistently low capacitance of Au polycrystalline electrodes (Au(poly)) was attributed to concentrated coverage of higher-energy Au(110) and Au(210) surfaces.

DC measurements demonstrated DMAP's facet-selective behavior on Au, prompting study of the necessary conditions to elicit anisotropic nanocrystal growth. Chloroauric acid (HAuCl$_4$) precursor and DMAP were allowed to react for a time (τ) before addition of sodium borohydride (NaBH$_4$) reducing agent. During the time before adding NaBH$_4$, a gradual change in solution color from orange to pale yellow indicated DMAP substitutes for chloride on the precursor molecule, and Au^{III} is gradually reduced to Au^{I}. By varying τ, the precursor oxidation state ratio (Au^{I}/Au^{III}) could be tuned, which in turn affected nanoparticle morphology (Fig. 3b). With $\tau = 0$, Au^{III}

was quickly and exhaustively reduced by NaBH$_4$, resulting in a burst of nucleating seeds without subsequent addition (Fig. 3c). An open-circuit potential (OCP) transient collected in the reaction solution (Fig. 3b) shows that the potential quickly returned to more positive potentials with NaBH$_4$ consumption. On the other hand, $\tau \geq 60$ min allowed for full conversion to Au^{I}, which is reduced much more slowly by NaBH$_4$ as evidenced by the sustained negative OCP (Fig. 3b). As a result of the slow reduction of Au^{I} by NaBH$_4$, Au^{0} sedimentation was observed rather than nanoparticle growth. At intermediate values of τ, anisotropic growth was observed due to a combination of quick nucleation from reduced Au^{III} and slow, thermodynamically-controlled addition from reduced Au^{I} (Fig. 3d and e). The transient for $\tau = 5$ min shows that the OCP rested primarily above −0.55 V *vs.* SCE during the first 14 min of the synthesis (Fig. 3b). Ultimately, the authors concluded that preferential adsorption of DMAP on Au(100) facets leads to overgrowth of Au(111) and anisotropic growth of nanopod structures. Though certainly useful for elucidating metal–ligand interactions, DC and chronocoulometric measurements are only able to provide thermodynamic evidence of facet-selective adsorption, whereas the shape of a nanostructure depends on the rate of atomic addition to different facets.

Additionally, evidence of preferential adsorption provides no indication of the effect of the ligand on the metal addition process as either passivating or enhancing, necessitating additional measurements of the redox processes resulting in anisotropic growth.

3. Mixed potential theory

Spontaneous electrochemical processes, including corrosion,[79,80] electroless plating,[81–83] and galvanic displacement,[84–86] consist of coupled oxidation and reduction reactions. In electroless plating techniques, oxidation of a reducing agent provides electrons for the reduction of metal ions. In galvanic displacement, oxidation of sacrificial metal substrates results in the reduction of more noble metal ions. Such redox processes have been explained using mixed potential theory, initially conceived by Wagner and Traud in 1938 to investigate corrosion.[79]

Mixed potential theory relies on the principle that the rate of electron production by oxidation reaction(s) is identical to the rate of consumption by reduction reaction(s) (stemming from conservation of charge). As a result, redox reactions occur spontaneously at a specific potential where these rates are identical, referred to as the mixed potential (E_{mp}) (Fig. 4a). Anodic and cathodic currents are equal and opposite at E_{mp}, and thus the net observed current for a given redox couple is zero. However, the reaction rate at E_{mp} is not zero and must be obtained from a Tafel plot (Fig. 4b). If the redox reaction is limited by charge transfer and not mass transport, extrapolation of the linear portions of the Tafel plot adhere to the Butler–Volmer equation, and their intersection at E_{mp} correspond to the reaction current of the redox process.

The growth of anisotropic metal nanocrystals (and metal nanoparticles more generally) results from spontaneous redox reactions in a manner similar to electroless plating. If growth occurs through atomic addition, reducing agents are oxidized on the surface of metal nanocrystal seeds, providing electrons for the reduction of metal ions, which subsequently add to the metal surface. In colloidal syntheses, shape-directing agents alter the activity of different crystal facets. Therefore, single-crystal electrodes can be used to model specific facets on the nanocrystal. By applying mixed potential theory to single-crystal electrodes, information on the facet-selective behavior of shape-directing agents and differential metal growth rates may be obtained. Herein, we review the use of such electrochemical measurements on single-crystal Cu electrodes to investigate the growth mechanism of Cu nanowires in two common syntheses using either alkylamines[43] or ethylenediamine (EDA)[42] as shape-directing agents.

3.1. Copper nanowire growth *via* competitive adsorption of alkylamines and chloride ions

Alkylamines are the most widely used shape-directing agents for Cu nanocrystals, enabling control of the shape of Cu nanocrystals with morphologies ranging from nanocubes to penta-
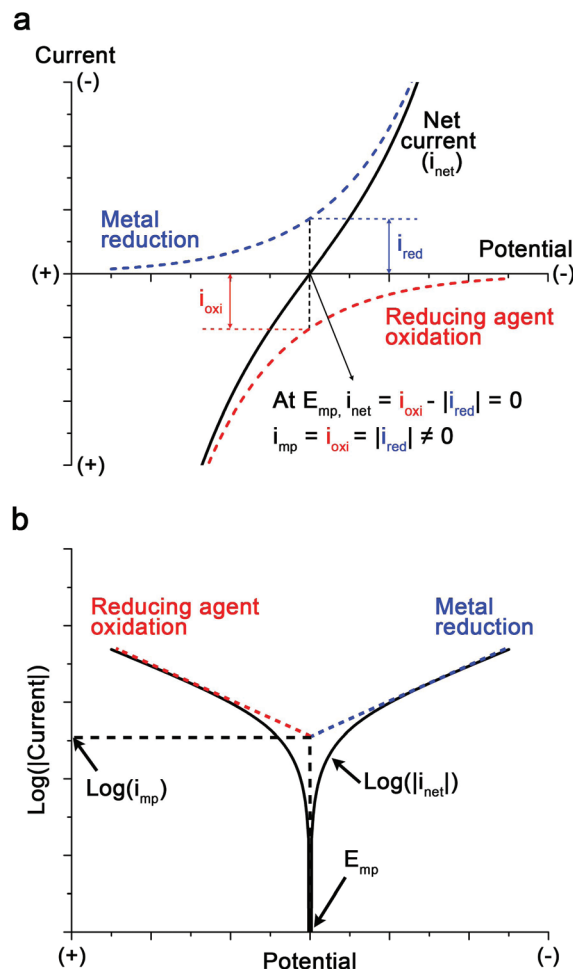

Fig. 4 (a) A diagram for mixed potential theory and (b) corresponding Tafel plot to obtain the current at the mixed potential. Reproduced with permission from ref. 43. Copyright 2018 American Chemical Society.

gonally-twinned nanowires.[31,87–89] In the case of pentagonally-twinned nanowires, the sides are thought to be sterically passivated to atomic addition by self-assembled monolayers (SAMs) of alkylamines, facilitating selective addition to {111} facets at the nanowire ends. However, this explanation leaves two critical questions unanswered: (1) why should alkylamines not adsorb on exposed {111} facets, and (2) why is the presence of chloride ions (Cl⁻) necessary for Cu nanowire syntheses to be successful?

With respect to the first question, density functional theory (DFT) has shown that the binding energies of hexadecylamine (HDA) to Cu(111) and Cu(100) surfaces are similar (1.86 and 1.97 eV, respectively).[90] Additionally, the concentration of alkylamines typically used is three-fold greater than that of the Cu ions, meaning there is sufficient ligand to cover all Cu surfaces produced during the synthesis.[31] In light of these facts, one could assert that facet-selective behavior from HDA should not occur.

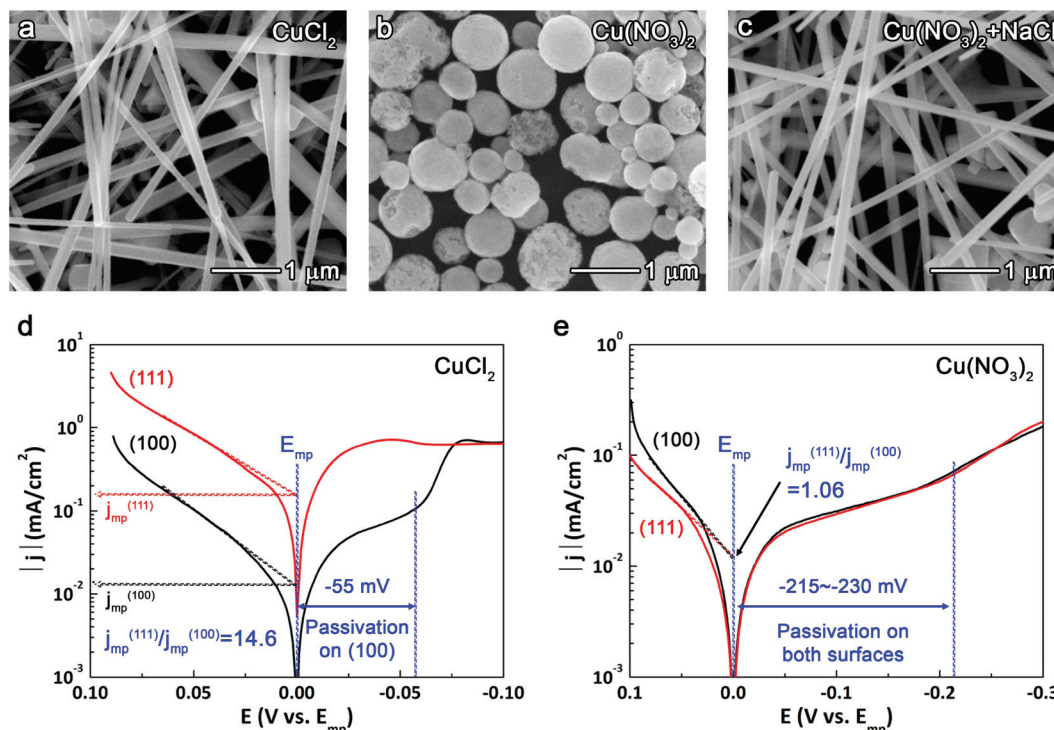With respect to the second question, it has been demonstrated that Cl⁻ is a necessary co-reagent with alkylamines for

Fig. 5 Cu nanocrystals synthesized from (a) CuCl$_2$, (b) Cu(NO$_3$)$_2$, and (c) Cu(NO$_3$)$_2$ and NaCl, all in the presence of HDA and ascorbic acid. Tafel plots collected on Cu(111) and Cu(100) single-crystal electrodes in the electrolytes of (d) CuCl$_2$ and (e) Cu(NO$_3$)$_2$ with HDA and ascorbic acid. Reproduced with permission from ref. 43. Copyright 2018 American Chemical Society.

anisotropic growth of Cu nanowires to occur (Fig. 5a–c),[43] yet the conventional mechanism does not immediately suggest what its role might be. In earlier studies, the significance of Cl$^-$ was likely obscured by the fact that CuCl$_2$ precursor is commonly used in alkylamine-assisted Cu nanowire syntheses. Chloride adsorbs on Cu surfaces with a binding energy greater than alkylamines, 3.31 eV for Cu(111) and 3.58 eV for Cu(100).[91] Moreover, it is known that Cl$^-$ adsorption affects subsequent adsorption of organic compounds.[92,93]

We recently investigated why Cl$^-$ is necessary for Cu nanowire growth with alkylamines using electrochemical measurements on Cu(111) and Cu(100) single-crystal electrodes.[43] Fig. 5d and e show Tafel plots collected in electrolytes with and without Cl$^-$ present. In the presence of both HDA and Cl$^-$, the greater current density on the Cu(111) surface relative to Cu(100) indicates that the rates of Cu^{1+}–alkylamine reduction and ascorbic acid oxidation were greater on the Cu(111) surface (Fig. 5d). In the absence of Cl$^-$, HDA passivated Cu(111) and Cu(100) surfaces to the comparable extent (Fig. 5e), eliminating the possibility of facet-selective passivation by HDA alone. These electrochemical findings agreed with the synthetic results in Fig. 5a–c, which show the formation of the Cu nanowires with Cl$^-$, and isotropic Cu nanoparticles without Cl$^-$.

To further test the relationship between the electrochemistry on the single-crystals and the nanowires, we investigated the effect of Cl$^-$ concentration on facet-selective atomic addition. This effect can be quantified by comparing the

current at the mixed potential (j_{mp}) for Cu(111) and Cu(100). The j_{mp} is obtained by extrapolating the linear portion of the Tafel plot to E_{mp}, the mixed potential at which the reaction occurs. This approach is valid for the alkylamine-mediated synthesis because nanowire growth in this synthesis is limited by charge transfer.[31] Fig. 6a and b show that the concentration of Cl$^-$ that maximized $j_{mp}^{(111)}$ relative to $j_{mp}^{(100)}$ was the same as the concentration that produced Cu nanowires with the highest aspect ratio. The strong correlation between the single-crystal electrochemistry and synthetic results indicated that similar facet-selective chemistry was likely occurring in both cases.

Further insight into why Cl preferentially displaced HDA from Cu(111) was provided by DFT calculations (Fig. 6c). Both Cu(100) and Cu(111) exhibited similar N–Cu bond distances (and thus similar bond strengths) in the absence of Cl, which explains the formation of spherical particles in the absence of Cl (Fig. 5b). At a Cl coverage of 0.25 monolayer (ML), the Cu–N interaction doubled in strength for Cu(100), but weakened for Cu(111). Increasing the Cl coverage to 0.33 ML resulted in weak physisorption of HDA on Cu(111) due to short-range repulsion between Cl and HDA, whereas the structure of Cu(100) accommodated strong chemisorption of both Cl and HDA. Higher concentrations of Cl displaced HDA from both facets.

The corroborating evidence from Cu nanowire synthesis, single-crystal electrochemistry, and DFT calculations provided strong support for the proposed growth mechanism illustrated in Fig. 6d. An intermediate concentration of Cl$^-$ led to selective desorption of HDA from the {111} facets at the ends of the Cu
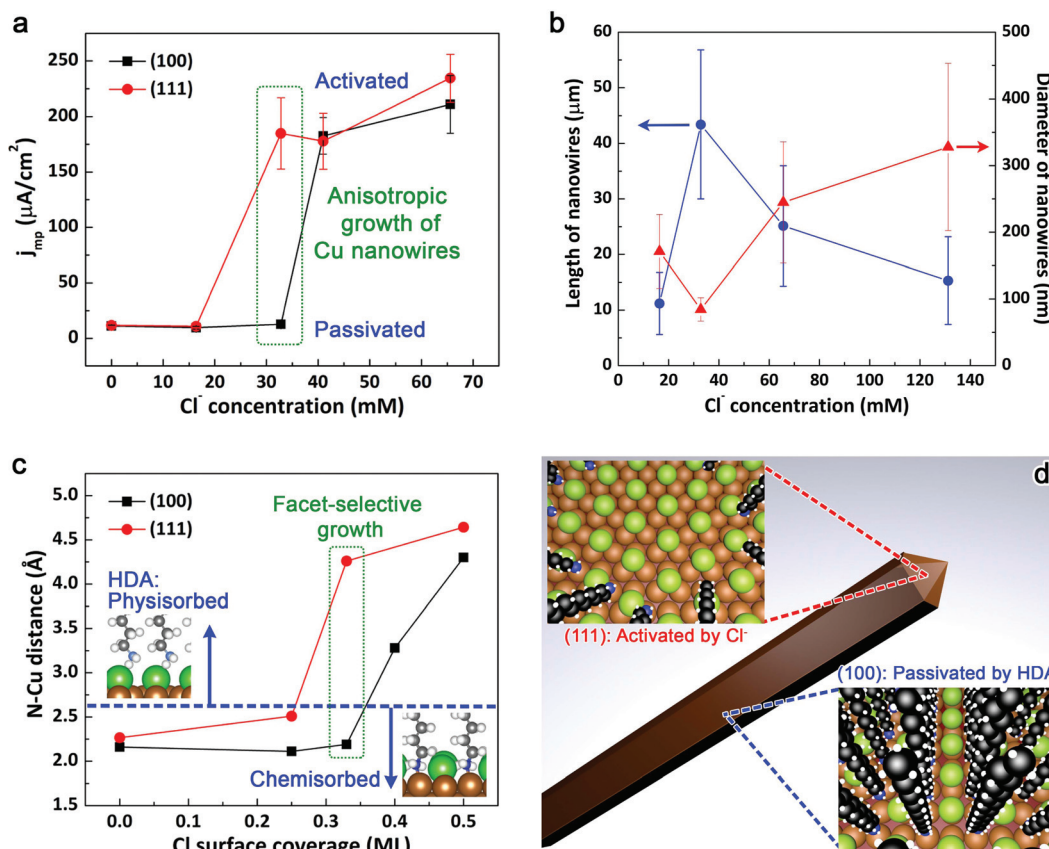
Fig. 6 (a) The current density at E_{mp} as a function of Cl$^-$ concentration. (b) The average length and diameter of Cu nanowires synthesized with varying Cl$^-$ concentrations. (c) N–Cu distance according to Cl surface coverage for Cu(100) and (111) surfaces. (d) A schematic for the growth of Cu nanowires in the presence of Cl$^-$ and HDA showing {111} facets at the ends of nanowires activated by Cl$^-$ for atomic addition and {100} facets on the sides completely passivated by the SAM of HDA. Reproduced with permission from ref. 43. Copyright 2018 American Chemical Society.

nanowires, thereby causing anisotropic growth. This work indicates the simple explanation of HDA acting as a facet-selective capping agent was incomplete. Instead, Cl$^-$ selectively displaced HDA from {111} facets.

3.2. Ethylenediamine promotes copper nanowire growth by inhibiting surface oxidation

Another method of synthesizing Cu nanowires is to reduce Cu–OH complexes with EDA as a shape-directing agent.[29,94–96] This synthesis does not require halide ions to achieve anisotropic growth, but it does require the use of a concentrated NaOH aqueous solution. Similar to the alkylamine-based synthesis, the growth of Cu nanowires has been previously described by preferential adsorption of EDA on {100} facets,[97] but there was no direct experimental evidence to support this hypothesis. We used mixed potential theory and single-crystal electrodes to show that EDA is not a capping agent, it is a facet-selective promoter of Cu deposition.[42]

Since Cu is oxidized in alkaline solutions, both reduction of a Cu(OH)$_2^-$ complex to Cu^0 and surface oxide compete with each other to take electrons produced from the oxidation of the reducing agent, N$_2$H$_4$. Based on mixed potential theory, the sum of the electrons consumed for both reduction reactions should equate to the amount produced by the oxidation of reducing agent (Fig. 7a). Therefore, we adopted electrochemical quartz crystal microbalance (EQCM) and chronoamperometry to separate the two reduction reactions and determine the mixed potential for Cu reduction.[42] Mass changes monitored by EQCM enabled the determination of the current for Cu(OH)$_2^-$ reduction $(i_{Cu(OH)_2^-})$, as well as the reaction potential. The current for the oxidation of N$_2$H$_4$ at the reaction potential was obtained by chronoamperometry in the solution without Cu ions. Based on mixed potential theory, this oxidation current was equivalent to the total reduction current $(i_{Cu(OH)_2^-} + i_{oxide})$. The faradaic efficiency for each reduction reaction was calculated with these two values (also see eqn (5)).[42] On polycrystalline Cu, only 27% of electrons from the reducing agent were consumed for reduction of Cu(OH)$_2^-$, and the remaining 73% went towards reduction of Cu oxide (Fig. 7).[42] This result demonstrates that surface oxidation should play an important role in the growth of Cu nanowires.

The rate of Cu deposition in the NaOH-EDA reaction is mass transport-limited[29,42] and competes with reduction of Cu oxide, so we could not apply the Tafel plot method introduced in section 3.1. Instead, we monitored the open circuit potential (OCP) of Cu single-crystal electrodes in reaction solutions with
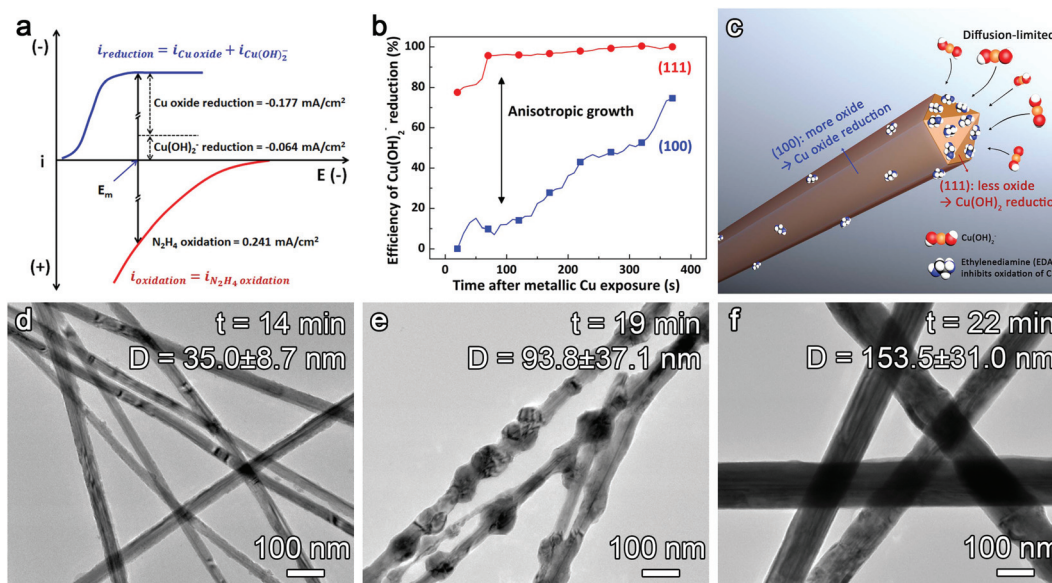
Fig. 7 (a) A diagram for mixed potential theory for EDA-based Cu nanowire growth. (b) Faradaic efficiency of $Cu(OH)_2^-$ reduction to Cu^0 on Cu(111) and Cu(100) single-crystal electrodes. (c) Growth mechanism of Cu nanowires in the presence of EDA and NaOH. TEM images of Cu nanowires at (d) 14 min, (e) 19 min, and (f) 22 min after starting the reaction. (a)–(c) are reproduced with permission from ref. 42. Copyright 2017 American Chemical Society. (d)–(f) are reproduced with permission from ref. 30. Copyright 2014 Royal Society of Chemistry.

and without Cu ions and converted these potentials into currents using an *i–V* curve for N_2H_4 oxidation.[42] Note that the OCP is the same as the mixed potential. The current for reduction of both surface oxide and $Cu(OH)_2^-$ $(i_{Cu(OH)_2^-} + i_{oxide})$ was obtained from the OCP of a solution containing NaOH, EDA, N_2H_4, and Cu ions, and the current for surface oxide reduction alone (i_{oxide}) was obtained from the same solution without Cu ions. The difference between these currents gives $i_{Cu(OH)_2^-}$, and the faradaic efficiency for $Cu(OH)_2^-$ to Cu^0 can be calculated using the following equation.[42]

$$\text{Faradaic efficiency}(\%) = \frac{i_{Cu(OH)_2^-}}{i_{Cu(OH)_2^-} + i_{oxide}} \times 100 \qquad (5)$$

Fig. 7b shows the faradaic efficiency for reduction of $Cu(OH)_2^-$ on Cu(111) and Cu(100) single-crystal electrodes. Most of the cathodic current (>80%) corresponded to Cu deposition on the Cu(111) surface, while electrons went primarily towards surface oxide reduction on the Cu(100) surface. This result shows that facet-selective Cu addition to {111} facets occurs in this reaction because reduction on {100} facets is blocked by surface oxide. This mechanism is illustrated in Fig. 7c. Fig. 7b also indicates the faradaic efficiency of Cu deposition on (100) became comparable to that on (111) after ~5 minutes, meaning atomic addition can also occur on the sides of nanowires after this period. It was previously observed that ~5 minutes after Cu nanowires form, additional Cu can deposit on the sides of the nanowires (see Fig. 7d–f).[30] The similar time-dependence for facet-selective Cu deposition on the single-crystals and the nanowires suggested similar chemistry is occurring in both cases.

The remaining question is why {111} facets were relatively free of surface oxide while {100} facets were blocked by surface oxides? Previous DFT calculations suggested that EDA adsorbed on the Cu surface could interrupt the adsorption of OH^- and prevent surface oxidation.[98] XPS analyses also suggested that EDA suppressed the oxidation of Cu.[98] However, the facet-dependent behavior of EDA was not experimentally confirmed. To address this question, we compared the OCP on Cu(111) and Cu(100) in solutions containing NaOH and N_2H_4 with or without EDA. Without EDA, the OCP becomes more negative over time as the surface oxide is reduced by N_2H_4 in a similar manner for both Cu(111) and Cu(100) (Fig. 8a). With EDA, the OCP becomes more negative about 5 minutes more quickly for Cu(111) then for Cu(100) (Fig. 8b). We concluded that EDA preferentially adsorbs to Cu(111) and thereby prevents surface oxidation. However, rather than having a passivating effect, the presence of EDA increases the current for N_2H_4 oxidation on Cu(111) to a greater extent than Cu(100), and the oxidation current increases with the concentration of EDA (Fig. 8c and d). These results indicate that, by keeping the Cu(111) surface free of oxides, EDA acts as a facet-selective promoter for Cu deposition rather than a capping agent. By keeping the ends of growing Cu nanowires free of surface oxides, EDA promoted anisotropic growth (Fig. 7c).

4. Measurements with single-crystal electrodes

Electrochemical measurements with single-crystal electrodes may pose a challenge to those not experienced with electro-
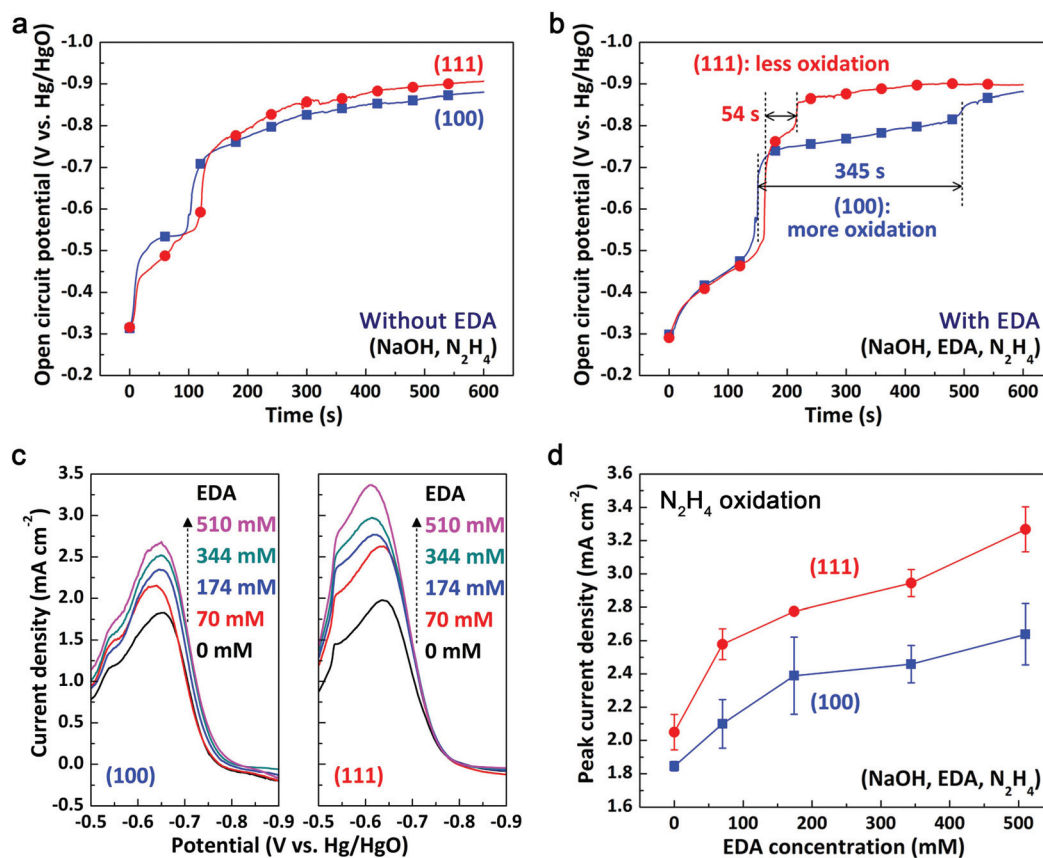
Fig. 8 The changes in open circuit potential of Cu(111) and Cu(100) single-crystal electrodes in NaOH solutions containing (a) N_2H_4 and (b) EDA-N_2H_4. (c) Linear sweep voltammograms and (d) the peak current density for N_2H_4 oxidation on Cu(111) and Cu(100) single-crystal electrodes as a function of EDA concentration. Reproduced with permission from ref. 42. Copyright 2017 American Chemical Society.

chemical techniques, and the data must be interpreted with caution. When electrochemical findings appear to contradict previous hypotheses based on synthetic results, one must verify that the discrepancy does not simply result from experimental errors. Herein, we include some common problems encountered in the course of collecting electrochemical data with single-crystal electrodes and how they can be avoided or resolved.

4.1. Electrode preparation and surface pretreatment

Electrochemical equipment vendors do not typically provide mounted single-crystal electrodes (*e.g.*, in the form of standard disk electrodes). However, many single-crystal metals are commercially available—commonly in the shape of a disk. Briefly, the metal disk is pressed into a non-conductive jacket (*e.g.*, PEEK tubing) to expose only the side of desired crystallinity, and the gap between the PEEK tubing and metal disk is filled with a non-conductive epoxy. An electrical connection between the back of the disk and a Cu wire is made with a Ag conductive epoxy or soldering. The Cu wire and the back side of metal disk are coated with a non-conductive, watertight epoxy to prevent contact with the reaction solution. The non-conductive

epoxy should be chosen to be compatible with the reaction solution (*e.g.*, pH and temperature). There should be little electrical resistance (<0.2 Ω) between the exposed single-crystal electrode and the lead. If the electrode is continuously used at high temperatures (*e.g.*, >60 °C), the electrical resistance should be periodically measured as the different thermal expansion coefficients of epoxy and metal may cause loss of electrical contact.

The surface of a working electrode must be smooth and free of contaminants in order to collect accurate electrochemical data, necessitating a number of surface pretreatment procedures between measurements. Mechanical polishing using a diamond or alumina slurry on a microfiber pad, followed by careful washing and sonication, is generally sufficient for restoring polycrystalline electrodes and obtaining reproducible data. However, single-crystal electrodes should ideally be as smooth as possible (approaching atomically smooth) to minimize the number of step edges and other surface defects and ensure uniform crystallinity.

Electropolishing and etching procedures may be used to further restore and clean single-crystal electrode surfaces. In electropolishing, the electrode may be repeatedly cycled between anodic and cathodic potentials in acid (*e.g.*, sulfuric,

phosphoric, perchloric acid) to strip surface contaminants and reduce roughness. The last cycle of electropolishing should finish at the cathodic limit to clear the surface of metal oxides. Electrochemical etching typically involves anodic polarization of the electrode in an etchant solution, which causes dissolution of exposed surface atoms. Chemical etching is similar but occurs spontaneously (*i.e.*, without the need for a driving potential). Etching procedures are particularly useful in experiments involving metal addition to single-crystal electrodes, as the deposited metal layer must be removed between measurements to restore the surface structure.

Electrochemical etching in concentrated phosphoric acid (+1.6 V *versus* Pt cathode) yields smooth Cu single crystals.[99] Gold can be electrochemically etched in concentrated solutions of potassium iodide with anodic polarizations, although stabilizing reagents such as sodium sulfite are required to reverse the formation of iodine (I_2).[100] Additionally, electropolishing after etching is necessary to remove surface-adsorbed iodide. Silver can be chemically etched in a solution of chromium trioxide and hydrochloric acid, followed by washes with concentrated ammonia and finally sulfuric acid.[58,101]

After the polishing step, it is necessary to check the surface crystal structure to validate the polishing method. Although scanning tunneling microscopy (STM) can confirm the surface structure, it can be used only over a very small area, and the shape and size of electrode can make it difficult to perform STM. Electrochemical measurements for adsorption of ions (*e.g.*, halide ions, hydroxyl ions),[102,103] small molecules,[104–106] and gaseous species (*e.g.*, CO),[107] or underpotential deposition[108] can be alternatively used because these phenomena are affected by the surface crystallinity. For example, the current spike in a cyclic voltammogram for the phase transition of sulfate ions was only observed on a Au(111) single-crystal electrode in sulfuric acid, but no current spike was observed with a Au(100) single-crystal electrode.[109] In addition, if the orientation of single-crystal electrodes is already confirmed by X-ray diffraction (XRD), surface area measurement can be used to compare polishing methods. The ideal polishing method should result in a surface area that closely matches the geometric surface area of the electrode.

4.2. Reaction solution preparation and data acquisition

A typical nanocrystal synthesis reaction solution is composed of a solvent, a metal precursor, reducing agent, and one or more shape-directing agents. The effect of each chemical component on nanocrystal morphology can be clarified by varying their individual concentrations. However, in electrochemical measurements, changing these concentrations may also alter the solution resistance. If the solution resistance is extremely high, as occurs when the electrolyte concentration is low, there will be a substantial ohmic drop between the working and reference electrodes which will introduce inaccuracies in the application and measurement of potentials. One solution to this problem is IR compensation, a function built into most commercial potentiostats. Alternatively, the addition of supporting electrolyte to the reaction solution will minimize this

ohmic drop. An appropriate electrolyte should be inert so it will not affect the electrochemical reactions under observation. The effect of the electrolyte on the growth of the metal nanostructures should also be determined by imaging any changes in nanostructure morphology that occur upon addition of the electrolyte. To simplify the experiment, ideally there should be no effect of the electrolyte on nanostructure morphology. In our previous study of Cu nanowire growth, potassium nitrate (KNO_3) was used,[43] and Burgess *et al.* have used sodium fluoride (NaF) in their studies of Au nanocrystal growth.[70,71]

During nanocrystal growth, each crystal facet of a nanocrystal will eventually reach an equilibrium coverage of adsorbates when the rates of adsorption and desorption are equal. Adsorption of species at the electrode surface alters the open circuit potential (OCP). Changes in the OCP can be used to observe time-dependent changes at the electrode–solution interface and determine the point at which equilibrium has been achieved (*i.e.*, when the OCP value has stabilized).[43] For example, the time to reach this equilibrium was previously observed to be 100 s for the Cu nanowire growth solution with HDA and Cl$^-$, so electrochemical measurements were started 300 s after dipping the electrode in the reaction solutions.[43] However, the OCP can also change due to consumption of reactants in the solution, and such changes can potentially interfere with measurements of surface adsorbates if the reaction is fast. Measurements of the currents for facet-selective atomic addition should be carried out after the coverage of adsorbates has reached an equilibrium coverage to reflect the surface coverage that is present on the surface of metal nanostructures in solution.

For measurements of reaction kinetics (see section 3), the OCP corresponds to the mixed potential (E_{mp}), and Tafel plot voltammograms should ideally be collected over a range centered at this potential. The appropriate scan rate over this range must be optimized for a particular synthesis. The scan rate should be slow enough to minimize contributions from the capacitive current, but fast enough to collect data before the single-crystal surface has been substantially altered by metal deposition.

Data collection may be hampered by homogenous nanoparticle formation in the growth solution, often indicated by a color change. These off-electrode reactions are undesirable because they consume reagents and can lead to particle deposition on the electrode. In such instances, tuning of the reagents and their concentrations may be necessary (*e.g.*, using a less potent reducing agent). Reducing the reaction temperature, verifying solution purity, and using thoroughly cleaned glassware are additional options.

Another limitation to the type of reaction that can be monitored is that the reducing agent should be added rather than generated *in situ*. For example, some Cu nanocrystal syntheses use glucose to reduce Cu ions, but glucose by itself does not act as a reducing agent. The Maillard reaction between alkylamines and glucose is necessary for generating the reductones capable of reducing Cu–alkylamine complexes.[31,110] The polyol process is another example in which the reducing agent is gen-

erated upon heating.[111] Fluctuations in the reducing agent concentration as it is generated and consumed make extracting reproducible kinetic data very difficult. In addition, the exact concentration of the reducing agent in such syntheses can be difficult to determine. Such limitations can be overcome by switching the reducing agent to one that can immediately act as a reducing agent by itself without intermediate reactions. For example, glucose can be replaced with ascorbic acid in a Cu nanowire synthesis to simplify the analysis of the facet-selective redox reactions.[43]

5. Summary and outlook

This review introduces how electrochemical measurements with single-crystal electrodes can be used to model and investigate the growth mechanism of anisotropic metal nanostructures. Measurements of differential capacitance and chronocoulometric techniques on single-crystal electrodes can determine whether organic additives preferentially adsorb to a given crystal facet, and whether the presence of halides affects such adsorption. The facet-dependent rate of reduction and oxidation reactions in a nanostructure growth solution can be analyzed using single-crystal electrodes and mixed potential theory. These kinetic measurements have already shown that the facet-selective capping agent hypothesis does not apply in two separate syntheses of Cu nanowires. In one, Cl⁻ promotes addition of Cu atoms to the ends of a growing nanowire by selectively displacing alkylamines from {111} facets. In another synthesis, EDA promotes addition of Cu atoms to the end of a growing nanowire by selectively preventing oxidation of Cu on {111} facets.

Despite the potential of single-crystal electrochemistry to answer longstanding questions of whether organic additives preferentially bind to and block atomic addition to certain facets of a metal nanostructure, there have as of yet been only a few studies that use single-crystal electrochemistry to address these questions. There remain many nanostructure syntheses for which similar techniques could be applied to determine the facet-selective chemistry causing anisotropic growth. Interpretation of these experimental results will be aided by computer simulations that can provide an atomic-level picture of the electrochemical interface. The deeper understanding provided by such studies will enable the development of more robust syntheses that produce nanostructure products in higher yields, as well as aid the development of synthesis that produce new nanostructures with novel properties.

Conflicts of interest

The authors declare no competing financial interests.

Acknowledgements

References

1 D. Huo, M. J. Kim, Z. Lyu, Y. Shi, B. J. Wiley and Y. Xia, *Chem. Rev.*, 2019, **119**, 8972–9073.

2 K. D. Gilroy, A. Ruditskiy, H. C. Peng, D. Qin and Y. Xia, *Chem. Rev.*, 2016, **116**, 10414–10472.

3 X. Yang, M. Yang, B. Pang, M. Vara and Y. Xia, *Chem. Rev.*, 2015, **115**, 10410–10488.

4 N. S. Porter, H. Wu, Z. Quan and J. Fang, *Acc. Chem. Res.*, 2013, **46**, 1867–1877.

5 D. Wang and Y. Li, *Adv. Mater.*, 2011, **23**, 1044–1060.

6 M. J. Kim, M. A. Cruz, F. Yang and B. J. Wiley, *Curr. Opin. Electrochem.*, 2019, **16**, 19–27.

7 Y. Xia, Y. Xiong, B. Lim and S. E. Skrabalak, *Angew. Chem., Int. Ed.*, 2009, **48**, 60–103.

8 P. Liu, R. Qin, G. Fu and N. Zheng, *J. Am. Chem. Soc.*, 2017, **139**, 2122–2131.

9 A. R. Tao, S. Habas and P. Yang, *Small*, 2008, **4**, 310–325.

10 M. Grzelczak, J. Pérez-Juste, P. Mulvaney and L. M. Liz-Marzán, *Chem. Soc. Rev.*, 2008, **37**, 1783–1791.

11 M. R. Langille, M. L. Personick, J. Zhang and C. A. Mirkin, *J. Am. Chem. Soc.*, 2012, **134**, 14542–14554.

12 S. Mourdikoudis and L. M. Liz-Marzán, *Chem. Mater.*, 2013, **25**, 1465–1476.

13 B. Wiley, Y. Sun, B. Mayers and Y. Xia, *Chem. – Eur. J.*, 2005, **11**, 454–463.

14 B. Wiley, Y. Sun and Y. Xia, *Acc. Chem. Res.*, 2007, **40**, 1067–1076.

15 Y. Sun, B. Gates, B. Mayers and Y. Xia, *Nano Lett.*, 2002, **2**, 165–168.

16 C. J. Murphy, T. K. Sau, A. M. Gole, C. J. Orendorff, J. Gao, L. Gou, S. E. Hunyadi and T. Li, *J. Phys. Chem. B*, 2005, **109**, 13857–13870.

17 L. Gou and C. J. Murphy, *Chem. Mater.*, 2005, **17**, 3668–3672.

18 J. Perez-Juste, I. Pastoriza-Santos, L. M. Liz-Marzán and P. Mulvaney, *Coord. Chem. Rev.*, 2005, **249**, 1870–1901.

19 M. Wu, A. M. Vartanian, G. Chong, A. K. Pandiakumar, R. J. Hamers, R. Hernandez and C. J. Murphy, *J. Am. Chem. Soc.*, 2019, **141**, 4316–4327.

20 Z. Hens and J. C. Martins, *Chem. Mater.*, 2013, **25**, 1211–1221.

21 L. E. Marbella and J. E. Millstone, *Chem. Mater.*, 2015, **27**, 2721–2739.

22 S. D. Techane, L. J. Gamble and D. G. Castner, *J. Phys. Chem. C*, 2011, **115**, 9432–9441.

23 M. D. Torelli, R. A. Putans, Y. Tan, S. E. Lohse, C. J. Murphy and R. J. Hamers, *ACS Appl. Mater. Interfaces*, 2015, **7**, 1720–1725.

24 H.-G. Liao, L. Cui, S. Whitelam and H. Zheng, *Science*, 2012, **336**, 1011–1014.

25 X. Ye, M. R. Jones, L. B. Frechette, Q. Chen, S. C. Nguyen, V. P. Adiga, A. Zettl, E. Rabani, P. L. Geissler and A. P. Alivisatos, *Science*, 2016, **354**, 874–877.

26 Y. Sun and Y. Wang, *Nano Lett.*, 2011, **11**, 4386–4392.

27 Y. Sun, *Mater. Today*, 2012, **15**, 140–147.

28 L. Yu, Z. Yan, Z. Cai, D. Zhang, P. Han, X. Cheng and Y. Sun, *Nano Lett.*, 2016, **16**, 6555–6559.

29 S. Ye, Z. Chen, Y.-C. Ha and B. J. Wiley, *Nano Lett.*, 2014, **14**, 4671–4676.

30 S. Ye, A. R. Rathmell, I. E. Stewart, Y.-C. Ha, A. R. Wilson, Z. Chen and B. J. Wiley, *Chem. Commun.*, 2014, **50**, 2562–2564.

31 M. J. Kim, S. Alvarez, T. Yan, V. Tadepalli, K. A. Fichthorn and B. J. Wiley, *Chem. Mater.*, 2018, **30**, 2809–2818.

32 J.-W. Lee, J. Han, D. S. Lee, S. Bae, S. H. Lee, S.-K. Lee, B. J. Moon, C.-J. Choi, G. Wang and T.-W. Kim, *Small*, 2018, **14**, 1703312.

33 H. J. Yang, S. Y. He, H. L. Chen and H. Y. Tuan, *Chem. Mater.*, 2014, **26**, 1785–1793.

34 Z. Chen, T. Balankura, K. A. Fichthorn and R. M. Rioux, *ACS Nano*, 2019, **13**, 1849–1860.

35 S. Zhou, J. Li, K. D. Gilroy, J. Tao, C. Zhu, X. Yang, X. Sun and Y. Xia, *ACS Nano*, 2016, **10**, 9861–9870.

36 Q. Zhang, W. Li, C. Moran, J. Zeng, J. Chen, L.-P. Wen and Y. Xia, *J. Am. Chem. Soc.*, 2010, **132**, 11372–11378.

37 Y. Wang, Y. Zheng, C. Z. Huang and Y. Xia, *J. Am. Chem. Soc.*, 2013, **135**, 1941–1951.

38 J. S. Duchene, W. Niu, J. M. Abendroth, Q. Sun, W. Zhao, F. Huo and W. D. Wei, *Chem. Mater.*, 2013, **25**, 1392–1399.

39 T. K. Sau and C. J. Murphy, *J. Am. Chem. Soc.*, 2004, **126**, 8648–8649.

40 M. L. Personick, M. R. Langille, J. Zhang, N. Harris, G. C. Schatz and C. A. Mirkin, *J. Am. Chem. Soc.*, 2011, **133**, 6170–6173.

41 H. L. Wu, C. H. Chen and M. H. Huang, *Chem. Mater.*, 2009, **21**, 110–114.

42 M. J. Kim, P. F. Flowers, I. E. Stewart, S. Ye, S. Baek, J. J. Kim and B. J. Wiley, *J. Am. Chem. Soc.*, 2017, **139**, 277–284.

43 M. J. Kim, S. Alvarez, Z. Chen, K. A. Fichthorn and B. J. Wiley, *J. Am. Chem. Soc.*, 2018, **140**, 14740–14746.

44 M. S. Bakshi, *Cryst. Growth Des.*, 2016, **16**, 1104–1133.

45 C. J. Murphy, L. B. Thompson, D. J. Chernak, J. A. Yang, S. T. Sivapalan, S. P. Boulos, J. Huang, A. M. Alkilany and P. N. Sisco, *Curr. Opin. Colloid Interface Sci.*, 2011, **16**, 128–134.

46 S. Bhanushali, P. Ghosh, A. Ganesh and W. Cheng, *Small*, 2015, **11**, 1232–1252.

47 M. Bobinger, J. Mock, P. La Torraca, M. Becherer, P. Lugli and L. Larcher, *Adv. Mater. Interfaces*, 2017, **4**, 1700568.

48 S. E. Lohse, N. D. Burrows, L. Scarabelli, L. M. Liz-Marzán and C. J. Murphy, *Chem. Mater.*, 2014, **26**, 34–43.

49 H.-J. Yang, S.-Y. He and H.-Y. Tuan, *Langmuir*, 2014, **30**, 602–610.

50 J. Zeng, X. Xia, M. Rycenga, P. Henneghan, Q. Li and Y. Xia, *Angew. Chem., Int. Ed.*, 2011, **50**, 244–249.

51 N. D. Burrows, A. M. Vartanian, N. S. Abadeer, E. M. Grzincic, L. M. Jacob, W. Lin, J. Li, J. M. Dennison, J. G. Hinman and C. J. Murphy, *J. Phys. Chem. Lett.*, 2016, **7**, 632–641.

52 C. J. Murphy, A. M. Gole, S. E. Hunyadi and C. J. Orendorff, *Inorg. Chem.*, 2006, **45**, 7544–7554.

53 J. Lipkowski, C. N. Van Huang, C. Hinnen and R. Parsons, *J. Electroanal. Chem.*, 1983, **143**, 375–396.

54 J. Richer and J. Lipkowski, *J. Electroanal. Chem.*, 1988, **251**, 217–234.

55 L. Stolberg, J. Lipkowski and D. E. Irish, *J. Electroanal. Chem.*, 1987, **238**, 333–353.

56 L. Stolberg, J. Richer, J. Lipkowski and D. E. Irish, *J. Electroanal. Chem.*, 1986, **207**, 213–234.

57 C. N. Van Huong, *J. Electroanal. Chem.*, 1989, **264**, 247–258.

58 A. Hamelin, S. Morin, J. Richer and J. Lipkowski, *J. Electroanal. Chem.*, 1991, **304**, 195–209.

59 Z. Shi and J. Lipkowski, *J. Electroanal. Chem.*, 1996, **403**, 225–239.

60 D. C. Grahame, *J. Am. Chem. Soc.*, 1941, **63**, 1207–1215.

61 R. Parsons, *Chem. Rev.*, 1990, **90**, 813–826.

62 M. Proskurnin and A. Frumkin, *Trans. Faraday Soc.*, 1935, **31**, 110–115.

63 D. C. Grahame, *Chem. Rev.*, 1947, **41**, 441–501.

64 R. Schapink, *Proc. R. Soc. London, Ser. A*, 1961, **261**, 79–90.

65 J. Lipkowski and P. N. Ross, *Adsorption of molecules at metal electrodes*, VCH, New York, 1992.

66 F. C. Anson, *Anal. Chem.*, 1966, **38**, 54–57.

67 J. Richer and J. Lipkowski, *J. Electrochem. Soc.*, 1986, **133**, 121–128.

68 R. Parsons, *Trans. Faraday Soc.*, 1955, **51**, 1518–1529.

69 I. J. Burgess, in *Advances in Electrochemical Sciences and Engineering*, ed. R. C. Alkire, P. N. Bartlett and J. Lipkowski, 2017.

70 J. P. Vivek and I. J. Burgess, *Langmuir*, 2012, **28**, 5031–5039.

71 J. P. Vivek and I. J. Burgess, *Langmuir*, 2012, **28**, 5040–5047.

72 J. P. Vivek and I. J. Burgess, *J. Electroanal. Chem.*, 2010, **649**, 16–22.

73 J. P. Vivek, A. Monsur and I. J. Burgess, *Surf. Interface Anal.*, 2013, **45**, 1402–1409.

74 Z. Shi and J. Llpkowskl, *J. Electroanal. Chem.*, 1994, **369**, 283–287.

75 D. I. Gittins and F. Caruso, *Angew. Chem., Int. Ed.*, 2001, **40**, 3001–3004.

76 R. P. Briñas, M. Maetani and J. J. Barchi, *J. Colloid Interface Sci.*, 2013, **392**, 415–421.

77 B. C. Barlow and I. J. Burgess, *Langmuir*, 2007, **23**, 1555–1563.

78 B. R. Danger, D. Fan, J. P. Vivek and I. J. Burgess, *ACS Nano*, 2012, **6**, 11018–11026.

79 C. Wagner and W. Traud, *Z. Elektrochem. Angew. Phys. Chem.*, 1938, **44**, 391–402.

80 J. Li, T. K. Zhong and M. E. Wadsworth, *Hydrometallurgy*, 1992, **29**, 47–60.

81 P. Bindra and J. Roldan, *J. Appl. Electrochem.*, 1987, **17**, 1254–1266.

82 P. Bindra, D. Light and D. Rath, *IBM J. Res. Dev.*, 1984, **28**, 668–678.

83 T. Lim, K. J. Park, M. J. Kim, H.-C. Koo and J. J. Kim, *J. Electrochem. Soc.*, 2012, **159**, D724–D729.

84 L. A. Porter, H. C. Choi, A. E. Ribbe and J. M. Buriak, *Nano Lett.*, 2002, **2**, 1067–1071.

85 S. Ambrozik, B. Rawling, N. Vasiljevic and N. Dimitrov, *Electrochem. Commun.*, 2014, **44**, 19–22.

86 C. P. daRosa, E. Iglesia and R. Maboudian, *J. Electrochem. Soc.*, 2008, **155**, D244–D250.

87 M. Jin, G. He, H. Zhang, J. Zeng, Z. Xie and Y. Xia, *Angew. Chem., Int. Ed.*, 2011, **50**, 10560–10564.

88 H. Xiang, T. Guo, M. Xu, H. Lu, S. Liu and G. Yu, *ACS Appl. Nano Mater.*, 2018, **1**, 3754–3759.

89 D. V. Ravi Kumar, I. Kim, Z. Zhong, K. Kim, D. Lee and J. Moon, *Phys. Chem. Chem. Phys.*, 2014, **16**, 22107–22115.

90 S.-H. Liu, T. Balankura and K. A. Fichthorn, *Phys. Chem. Chem. Phys.*, 2016, **18**, 32753–32761.

91 S. Peljhan, J. Koller and A. Kokalj, *J. Phys. Chem. C*, 2014, **118**, 933–943.

92 G.-K. Liu, S. Zou, D. Josell, L. J. Richter and T. P. Moffat, *J. Phys. Chem. C*, 2018, **122**, 21933–21951.

93 S.-E. Bae and A. A. Gewirth, *Langmuir*, 2006, **22**, 10315–10321.

94 Y. Chang, M. L. Lye and H. C. Zeng, *Langmuir*, 2005, **21**, 3746–3748.

95 A. R. Rathmell and B. J. Wiley, *Adv. Mater.*, 2011, **23**, 4798–4803.

96 M. A. Cruz, S. Ye, M. J. Kim, C. Reyes, F. Yang, P. F. Flowers and B. J. Wiley, *Part. Part. Syst. Charact.*, 2018, **35**, 1700385.

97 A. R. Rathmell, S. M. Bergin, Y. L. Hua, Z. Y. Li and B. J. Wiley, *Adv. Mater.*, 2010, **22**, 3558–3563.

98 J. Koo, S. Kwon, N. R. Kim, K. Shin and H. M. Lee, *J. Phys. Chem. C*, 2016, **120**, 3334–3340.

99 T. P. Moffat and L.-Y. Ou Yang, *J. Electrochem. Soc.*, 2010, **157**, D228–D241.

100 Z. Hu and T. Ritzdorf, *J. Electrochem. Soc.*, 2007, **154**, D543–D549.

101 E. Lastraioli, F. Loglio, M. Cavallini, F. C. Simeone, M. Innocenti, F. Carla and M. L. Foresti, *Langmuir*, 2010, **26**, 17679–17685.

102 O. M. Magnussen, *Chem. Rev.*, 2002, **102**, 679–725.

103 B. M. Jovic, V. D. Jovic and G. R. Stafford, *Electrochem. Commun.*, 1999, **1**, 247–251.

104 D. F. Yang, C. P. Wilde and M. Morin, *Langmuir*, 1996, **12**, 6570–6577.

105 B. Roelfs, E. Bunge, C. Schröter, T. Solomun, H. Meyer, R. J. Nichols and H. Baumgärtel, *J. Phys. Chem. B*, 1997, **101**, 754–765.

106 M. H. Hölzle, T. Wandlowski and D. M. Kolb, *Surf. Sci.*, 1995, **335**, 281–290.

107 L. A. Kibler, A. Cuesta, M. Kleinert and D. M. Kolb, *J. Electroanal. Chem.*, 2000, **484**, 73–82.

108 E. Herrero, L. J. Buller and H. D. Abruña, *Chem. Rev.*, 2001, **101**, 1897–1930.

109 A. Cuesta, M. Kleinert and D. M. Kolb, *Phys. Chem. Chem. Phys.*, 2000, **2**, 5684–5690.

110 M. Kevin, G. Y. R. Lim and G. W. Ho, *Green Chem.*, 2015, **17**, 1120–1126.

111 S. E. Skrabalak, B. J. Wiley, M. Kim, E. V. Formo and Y. Xia, *Nano Lett.*, 2008, **8**, 2077–2081.